Soils and Foundations 2012;52(4):748–766

The Japanese Geotechnical Society

Soils and Foundations

www.sciencedirect.com
journal homepage: www.elsevier.com/locate/sandf

Stress–strain relations of cement-mixed gravelly soil from multiple-step triaxial compression test results ☆

A. Taheri[a,b], F. Tatsuoka[b,*]

[a]School of Civil, Environmental and Mining Engineering, The University of Adelaide, Australia
[b]Department of Civil Engineering, Tokyo University of Science, Japan

Received 2 January 2012; received in revised form 10 May 2012; accepted 20 June 2012
Available online 8 September 2012

Abstract

The peak compressive strengths at different confining pressures of cement-mixed gravel (CMG) that are very similar to those obtained by single-step loading (SL) drained triaxial compression (TC) tests using multiple specimens can be obtained by a multiple-step loading (ML) test using a single specimen. However, only the unload/reload stress–strain relations at different confining pressures (except for the primary loading pressure at the first step) can be obtained from an ML test, and the reloading relations become softer with the increases in negative irreversible axial strain increments that have taken place during the respective immediately preceding unloading regimes. This phenomenon is formulated by a unique empirical equation for the CMG tests. Undamaged reloading stress–strain curves (URCs) were inferred by removing the damage effects from measured reloading curves (MRCs) in the ML TC test based on this correlation. A method was developed within the framework of the proportional rule to infer primary loading curves (PLCs) at different confining pressures from the URCs and the PLC at the first step obtained from a given ML TC test. A procedure was formulated to modify the PLCs obtained by this procedure based on the PLCs measured at stresses exceeding the yield stress for large-scale yielding during reloading at different confining pressures in the ML test. This method was validated by comparing the PLCs obtained from the results of a pair of ML tests, increasing and decreasing the confining pressure, with those obtained from a set of SL TC tests at different confining pressures.

Keywords: Cement-mixed gravel; Multiple-step loading; Stress–strain relation; Triaxial compression test; Simulation (IGC D6/E13)

1. Introduction

The use of cement-mixed soil, produced by mixing soil with a relatively small amount of cement powder and a proper quantity of water, is now one of the most popular ground-improvement technologies. Compacted cement-mixed soil is often used to construct critical permanent soil structures by allowing very small deformation at the working loads. A number of related researches have been performed (e.g., Hansen and Reinhardt, 1990; Schrader, 1996; Tatsuoka et al., 1999). It has been revealed that the mechanical properties of cement-mixed soil are similar to those of natural sedimentary soft rock (Tatsuoka and Kohata, 1995; Tatsuoka et al., 1999). In 2003, the first bridge abutment, comprising the backfill of highly compacted cement-mixed gravelly soil (CMG) that supports a thin RC facing bearing a bridge girder, was constructed in Takada for a new high-speed train line in Kyushu, Japan (Aoki et al., 2003; Tatsuoka, 2004; Watanabe et al., 2005; Tatsuoka et al., 2005). Since that time (up to November 2011), nearly 60 similar bridge abutments have been constructed or are being

*Corresponding author.
E-mail address: tatsuoka@rs.noda.tus.ac.jp (F. Tatsuoka).
Peer review under responsibility of The Japanese Geotechnical Society

Production and hosting by Elsevier

0038-0806
http://dx.doi.org/10.1016/j.sandf.2012.07.014

Nomenclature

D_{50}	mean particle diameter
D_{max}	maximum particle diameter
E_{tan}	tangent Young's modulus
F_c	fines content
G_s	specific gravity of solid particles
U_c	uniformity coefficient
c/g	cement content per gravel weight
m	scaling factor
n	coefficient of proportionality for hysteresis stress–strain relations
q	deviator stress ($=\sigma'_v-\sigma'_h$)
q_{max}	maximum deviator stress
q_{peak}	peak strength
w_{opt}	optimum water content
w_i	water content
$(x_r)_R$	normalization factor of axial strain increment for reloading curves
$(x_r)_P$	normalization factor of axial strain increment for primary loading curves
$\varepsilon_{a(ave)}$	average axial strain
$\Delta\varepsilon_a$	axial strain increment
$\Delta\varepsilon_a^{ir}$	irreversible axial strain increment
$(\rho_d)_{max}$	maximum dry density
ρ_d	dry density
σ'_v	vertical (axial) effective stress
σ'_h	horizontal (lateral) effective stress

Abbriviated words

CL	cyclic loading
CMG	cement-mixed gravel
LDT	local deformation transducer
ML	multiple-step loading
MRC	measured reloading stress–strain curve
PLC	primary loading stress–strain curve
RL	reloading
SL	single-step loading
TC	triaxial compression
URC	undamaged reloading stress–strain curve

designed for construction, according to the Japan Railway Construction, Transport and Technology Agency.

Various factors, including the ageing effects at a shear stress on the subsequent stress–strain behavior and peak strength and the viscous effects on the stress–strain behavior, were studied by Kongsukprasert and Tatsuoka (2005, 2007), Tatsuoka et al. (2008), and Ezaoui et al. (2010). Moreover, the stress–strain behavior at different effective confining pressures (σ'_hs) of compacted CMG was evaluated extensively through stress–strain tests on specimens prepared in the laboratory (e.g., Watanabe et al., 2003, 2005; Kongsukprasert and Tatsuoka, 2003; Lohani et al., 2004; Kongsukprasert et al., 2005). It was found that the effects of σ'_h on the strength and the deformation characteristics are significant and, with a highly cohesive intercept, the angle of internal friction of the CMG could become nearly the same as, or even higher than, the value of the original unbound gravelly soil compacted in a similar manner. This fact indicates that CMG is not a purely cohesive material, but a complicated frictional/cohesive material with which not only the cohesive intercept (i.e., the shear strength at zero confining pressure), but also the frictional shear strength (i.e., the pressure-dependent shear strength component), increases by inter-particle bonding. The inter-particle bonding is continuously damaged during shearing, which is reflected in the measured non-linear stress–strain behavior during primary monotonic loading. In this study, the measured primary monotonic loading curves were analyzed without quantifying these damage effects; only the damage effects that took place during the immediately preceding unloading process on the reloading stress–strain curve were evaluated. It is beyond the scope of this paper to discuss these issues in further detail. To confidently evaluate the Mohr–Coulomb failure envelope of a given type of soil, we need to gather at least three, preferably four or five, very similar specimens. However, it is very difficult to accurately do so with CMG specimens retrieved from the field due to the high heterogeneity resulting mainly from the inevitably highly inhomogeneous on-site soil/cement/water mixing and the non-uniform vertical distribution of the compacted dry density in the respective lifts (Taheri et al., 2012). Although much more homogenous CMG can be obtained by mixing it in a plant on-site, this method is usually not adopted in ordinary-scale construction projects from the viewpoint of cost-effectiveness.

Taheri et al. (2012) showed that the peak strengths at different effective confining pressures (σ'_hs) and the associated Mohr–Coulomb failure criterion of moist compacted CMG, as obtained by a set of *single-step loading* (SL) drained TC tests at different σ'_hs using multiple similar specimens, can be inferred rather accurately from the results of a relevant *multiple-step loading* (ML) test using a single specimen. It was also confirmed that the effects of a full or partial unload/reload cycle made at a certain σ'_h on the peak strength, observed during the subsequent TC stage at an increased or decreased σ'_h, are generally negligible. On the other hand, the stress–strain relation during reloading at the same or a different σ'_h becomes softer with an increase in the amount of unloading and may become even softer than the corresponding primary loading stress–strain relation in an SL test under otherwise equal test conditions. In general, the reloading stress–strain relation of geomaterials becomes different

from that of the primary loading due to the following three factors (Taheri et al., 2011):

1. *Cyclic loading effect*, which composed of three components. The first is *the strain-hardening effect* associated with an expansion of the yield surface, by which the reloading stress–strain relation becomes substantially stiffer than that of the primary loading. The second is *the hysteresis effect*, by which the tangent modulus of the reloading stress–strain relation at the same shear stress decreases with an increase in the unloaded stress. The third is *the cyclic strain-hardening effect*, by which the stress–strain behavior becomes stiffer with an increase in the number of cyclic loadings along the same stress path. With bound materials, such as the CMG tested in this study, the effect of the third component is usually insignificant.
2. *Viscous effect*, by which the tangent modulus of CMG decreases with a decrease in the strain rate. This effect becomes more significant at higher shear stresses, especially when approaching the maximum stress states by reloading in the respective hysteresis loops.
3. *Effect of damage* that has taken place during the immediately preceding unloading, by which the tangent modulus at a given state during reloading decreases. This factor is particularly important with relatively weakly bound materials, such as the CMG tested in this study.

It is very convenient if a set of stress–strain curves during primary loading at different σ'_hs can be inferred, at least reasonably, from a given set of reloading stress–strain curves at these σ'_hs observed in an ML test using a single specimen. Previous studies on this subject cannot be found in any literature. The present study was performed for this objective based on the results of a series of drained TC tests on compacted CMG (Taheri et al., 2012). To this end, a method was developed within the framework of the proportional rule with the aim of applying it to general cases.

2. Test methods

The test material and the test method are described only briefly below, as detailed descriptions can be found in Taheri et al. (2012).

2.1. Specimens

Particles larger than 10 mm were removed from a well-graded gravelly quarry soil of crushed sandstone ($G_s=2.71$), called Chiba gravel, to obtain a test material having sub-angular particles with $G_s=2.74$, $D_{10}=0.171$ mm, $D_{50}=2.32$ mm, $U_c=19.0$, and $F_c=5.2\%$ (called "model Chiba gravel"). This gravelly soil was mixed with ordinary Portland cement at a cement-to-gravel ratio by dry weight (c/g) equal to 2.5%. A maximum dry density of $(\rho_d)_{max}=2.11$ g/cm^3 and an optimum water content of $w_{opt}=9.3\%$ were obtained by compaction tests (the standard Proctor) on the cement-mixed gravelly soil (CMG) performed before significant hydration had developed. To obtain TC specimens, the gravelly soil that had been mixed with air-dried cement powder was mixed with water at an initial water content of w_i (in the ratio to the dry weight of soil plus cement)$=8.75\%$, close to w_{opt}. The TC specimens, either rectangular prismatic (72 mm × 72 mm in cross-section and 150 mm high) or solid cylindrical (100 mm in diameter and 200 mm in height), were produced by manual compaction in five layers to a target compacted dry density ρ_d equal to 2.0 g/cm^3. The compacted specimens were cured under the atmospheric pressure at the same water content for a total period of 9 day. The difference between the two shapes of specimens used in this study, rectangular prismatic and solid cylindrical, had no significant effect on the results of the analysis presented in this paper. A separate study on the effects of the shape and the scale of specimens was performed by Ezaoui et al. (2011).

2.2. Triaxial compression test

To minimize the effects of non-uniform deformation and the associated non-uniform stress distribution within the specimen, due to irregular contact and high friction, the top and the bottom of the specimen set in a triaxial cell were made smooth by pasting a thin layer of gypsum slurry on them and by lubricating them by the smearing of a thin layer of silicon grease. The specimen was isotropically consolidated at $\sigma'_h=20$ kPa by means of partial vacuum. A set of local strain gauges (Local Deformation Transducers, LDTs, Goto et al., 1991) were installed in about 2 h, to accurately and sensitively evaluate the axial and lateral strains, along with other instrumentations. Solid rectangular specimens were used in drained triaxial compression tests performed to specifically measure sensitively and accurately the lateral strains free from bedding error effects at the specimen side faces taking place when the effective confining pressure changes by means of laterally placed LDTs (a total of six for each specimen; Ezaoui et al., 2010). Then, the following three series of drained TC tests were performed at an axial strain rate of 0.03%/minute.

1. Series 1: *Single-step loading* (SL) toward ultimate failure on specimens isotropically consolidated and cured for 2 h at different confining pressures, $\boldsymbol{\sigma}_h=\sigma'_h=0.02$ or 0.50 or 1.00 or 1.50 MPa. To evaluate the quasi-elastic properties, 10-minute unload/reload cycles were applied at several intermediate stages during otherwise continuous monotonic loading.
2. Series 2: Two *multiple-step loading* (ML) tests were performed by different methods:

   2(a): An ML test with full unloading of the deviator stress, $q=\sigma'_v-\sigma'_h$, followed by an increase in σ'_h: In the first step, at $\sigma'_h=0.02$ MPa, when sufficient irreversible deformation, which closely approached the peak stress

state, took place, TC loading was terminated. Then, q was reduced to zero and the specimen was left for 40 min to reach the equilibrium state. Then, σ'_h was increased to 0.25 MPa under isotropic stress conditions to perform the next step of TC loading. This procedure was repeated to perform TC loading at σ'_h =0.02, 0.25, 0.50, 0.75 and 1.0 MPa.

2(b): An ML test with full unloading of q followed by a decrease in σ'_h: In the first step, at σ'_h=1.0 MPa, when some large irreversible deformation, which closely approached the peak stress state, took place, TC loading was terminated. Then, q was reduced to zero and the specimen was left for 40 min to reach the equilibrium state. Then, σ'_h was decreased under isotropic stress conditions to 0.75 MPa to perform the next step of TC loading. This procedure was repeated to perform TC loading at σ'_h=1.0, 0.75, 0.50, 0.25 and 0.02 MPa.

In these two ML tests, drained TC loading at respective steps was stopped and reversed so that the total axial strain that would have taken place by the end of the final TC loading remained smaller than the measurable range of the axial LDTs (about 2.5%). Details of the test method and the test results are reported in Taheri et al. (2012).

3. Series 3: Cyclic loading to evaluate the cyclic loading effects on the stress–strain behavior during and after cyclic loading. Multiple unload/reload cycles, in which unloading was started from the same stress state followed by full reloading, were repeatedly applied increasing the deviator stress amplitude during otherwise continuous loading at a fixed σ'_h (0.02 or 0.50 or 1.0 MPa). In one of the tests, unloading was conducted until a triaxial extension stress state was reached.

3. Measured stress–strain relations

Single-step loading (*SL*) *tests* (*Series* 1): Fig. 1 shows the results of four drained SL TC tests at different σ'_h values. $\varepsilon_{a(ave)}$ denotes the axial strain obtained by averaging the axial strains locally measured with a pair of LDTs. The axial strain–volumetric strain relations from these and the other tests referred to in this paper are reported in Taheri et al. (2012). The peak strength does not increase in proportion to the confining pressure, indicating a large cohesive intercept with this material. The Mohr–Coulomb strength parameters from these tests are reported in Taheri et al. (2012). At the lowest σ'_h(=0.02 MPa), significant strain softening takes place after the peak stress state reaches a relatively small axial strain. With an increase in σ'_h, the axial strain at the peak stress state increases. These results serve as a reference for the Series 2 and 3 tests, described below.

Multiple-step loading (*ML*) *tests* (*Series* 2): Fig. 2(a) and (b) shows the results of a pair of ML tests increasing and decreasing σ'_h with the intermediate full unloading of q. The relationship between the strength characteristics

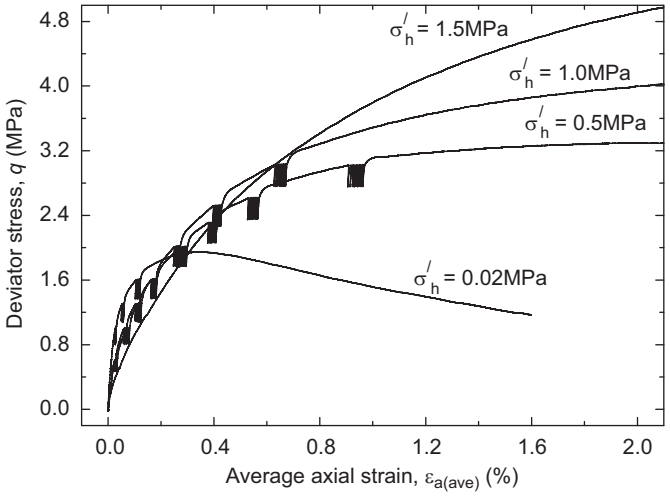

Fig. 1. Deviator stress–axial strain relations from SL drained TC tests (Series 1, rectangular prismatic specimens, Taheri et al., 2012).

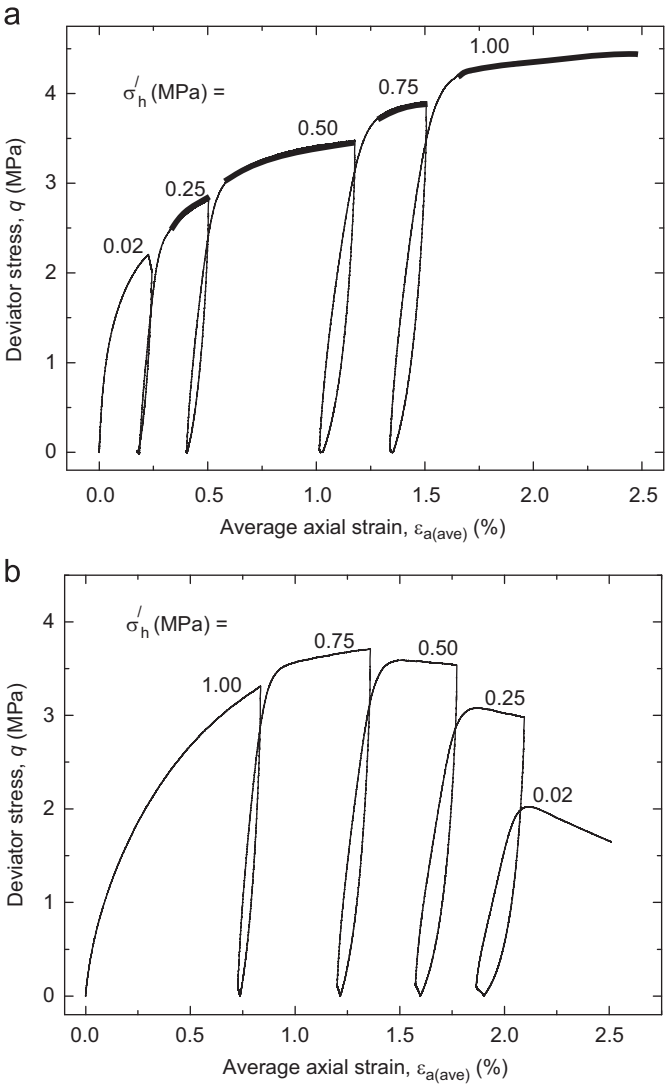

Fig. 2. Deviator stress–axial strain relations from ML drained TC tests (rectangular prismatic specimens): (a) increasing σ'_h (Series 2a) and (b) decreasing σ'_h (Series 2b) (Taheri et al., 2012).

(in particular, the pressure dependencies) from the results presented in Fig. 1 (a set of SL tests) and Fig. 2 (two ML tests) is analyzed in detail in Taheri et al. (2012). After having passed a yield point of the large-scale yielding during reloading, the stress–strain relation tends to rejoin the relation obtained by the SL tests at the same σ'_h. In Fig. 2(a), all stress–strain relations exhibit strain hardening toward the respective peak stress states after the start of large-scale yielding. Correspondingly, maximum deviator stress q_{max} at each step increases with an increase in σ'_h. The stress–strain relations after the large-scale yielding at the second and subsequent steps, which are denoted by thick black curves, are deemed to be free from the effects of the previous loading history, thereby showing essentially the

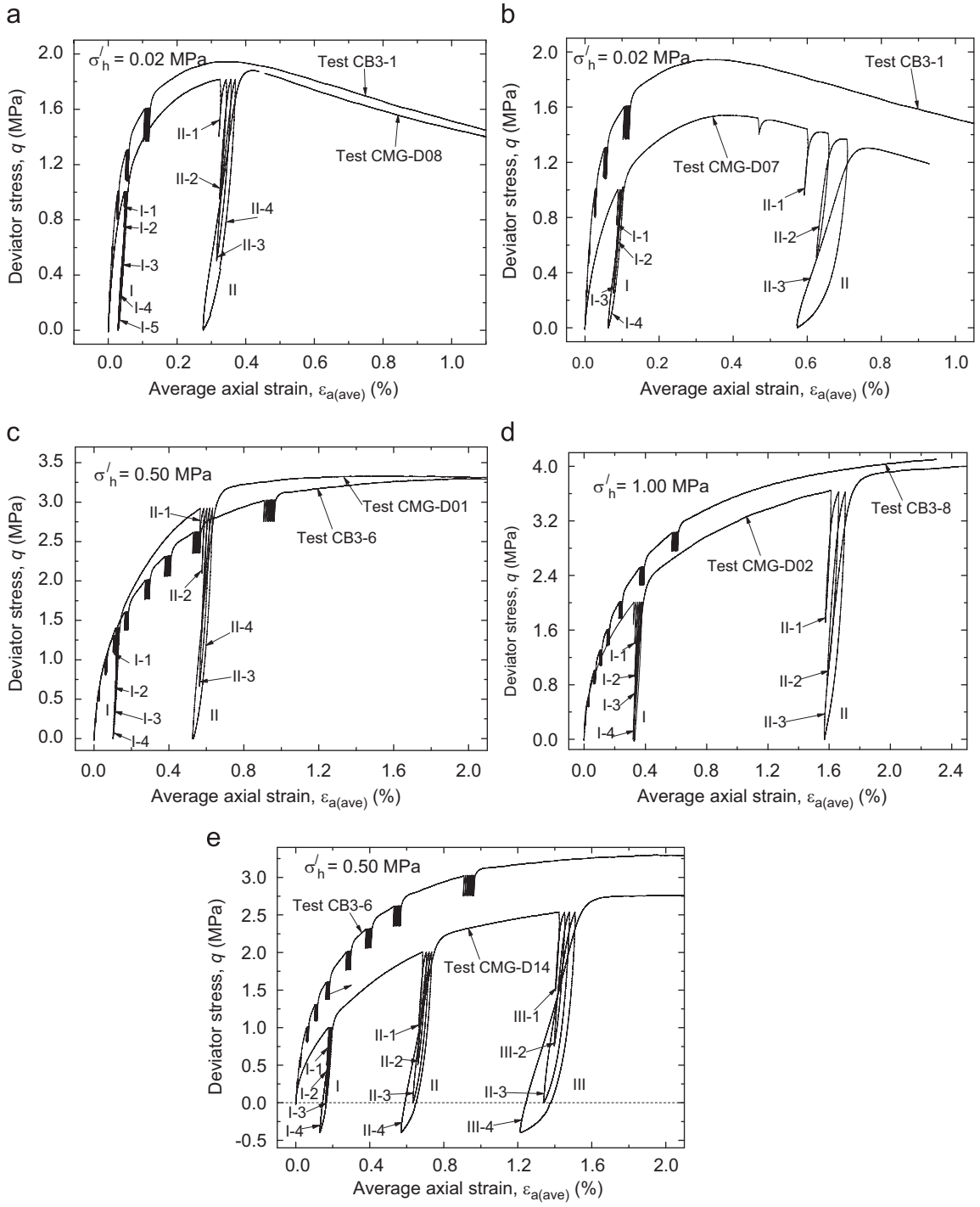

Fig. 3. Deviator stress–axial strain relations from TC tests with several unload/reload cycles (Series 3) (CMG-D in test names denotes Series 3) and continuous monotonic loading TC tests (Series 1) (CB in test names denotes Series 1): (a) Test CMG-D08 (SC) and CB3-1, σ'_h=0.02 MPa, (b) Test CMG-D07 (SC) and CB3-1, σ'_h=0.02 MPa, (c) Test CMG-D01 and CB3-6, σ'_h=0.50 MPa, (d) Test CMG-D02 and CB3-8, σ'_h=1.00 MPa, and (e) Test CMG-D14 (SC) and CB3-6, σ'_h=0.50 MPa (SC, solid cylindrical specimens).

same primary material behavior. In Fig. 2(b), on the other hand, despite a decrease in σ'_h, the q_{max} value at the second step ($\sigma'_h=0.75$ MPa) is larger than that at the first step ($\sigma'_h=1.0$ MPa). This is due to the fact that, at the first step, loading is terminated far before the peak stress state and, at the second step, the strain-hardening regime continues for a large axial strain increment after the start of the large-scale yielding. At the third and subsequent steps, the stress–strain behavior exhibits the noticeable trends of strain softening after the start of the large-scale yielding. Correspondingly, the q_{max} value at each step decreases significantly with a decrease in σ'_h.

Taheri et al. (2012) showed that the peak strengths at different σ'_h values and the associated Mohr–Coulomb failure criterion obtained by the SL tests at different σ'_h values using multiple similar specimens can be inferred rather accurately by these ML tests, respectively, using a single specimen and excluding the data from the TC steps terminated far before the peak strength. It is the objective of the present study to examine whether the primary pre-peak stress–strain relations at different σ'_hs, as obtained by a series of SL tests and the reloading stress–strain relations after unloading for given amounts of stress amplitude, can be inferred reasonably well from the results of such ML tests as those described above.

Cyclic loading tests (*Series* 3): Fig. 3 shows the results of a set of *cyclic loading* (CL) tests, compared with those from the SL tests at different σ'_hs (Series 1, Fig. 1). The details (i.e., names, test conditions, etc.) of these tests, and the others referred to in this paper, are reported in Taheri et al. (2012). After the start of the large-scale yielding during the last reloading toward ultimate failure, the stress–strain relation tends to rejoin the one obtained by the corresponding SL under otherwise equal conditions. Despite some scatter in the data, the peak strength does not decrease noticeably when applying several unload/reload cycles with relatively large stress amplitudes in these Series 3 tests. On the other hand, the stress–strain relation during reloading becomes noticeably softer with an increase in the deviator stress amplitude during the immediately preceding unloading regime. This trend is likely to be due to the effects of the damage that took place during the unloading. This trend is not observed with unbound granular materials. It is first necessary to evaluate this trend in behavior to accomplish the objectives of the present study.

4. Effects of damage on reloading stress–strain behavior

The tangent modulus at the same shear stress level during reloading decreases with an increase in the unloading increment not only by the damage effects that have taken place during the immediately preceding unloading stage, but also by the hysteresis effects (controlled by the amount of decrease in stress). To extract the damage effects, the hysteresis effects are removed from the test results based on the proportional rule, which is often employed to describe the hysteretic stress–strain (y–x) relations during the cyclic loading of unbound granular materials (e.g., Masuda et al., 1999; Tatsuoka et al., 2003; Fig. 4).

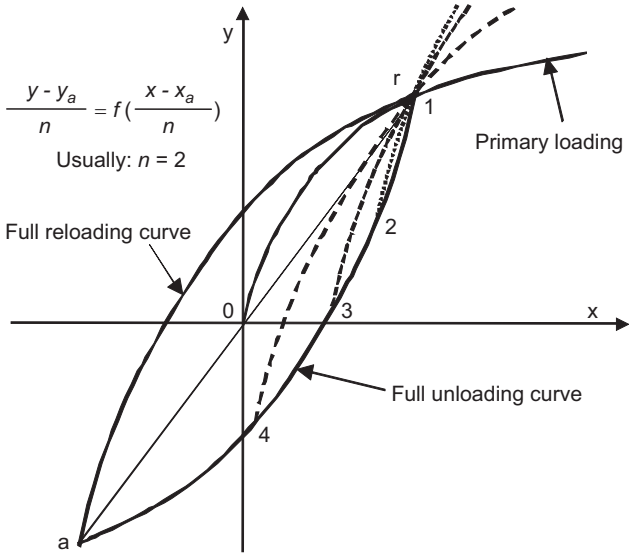

Fig. 4. Proportional rule not including cyclic strain-hardening effects, viscous effects or damage effects (Tatsuoka et al., 2003).

4.1. Proportional rule

According to this rule, when any of the cyclic strain-hardening effects, viscous effects or damage effects due to the large unloading are not included, the reloading stress–strain relation from a given stress–strain state (y_i, x_i) (such as points 2, 3 and 4 in Fig. 4) is obtained as

$$\frac{y-y_i}{n}=f\left(\frac{x-x_i}{n}\right) \tag{1}$$

where $y=f(x)$ is the primary stress–strain relation starting from origin *0* and n is the coefficient of proportionality, larger than unity. Eq. (1) is obtained by the parallel shifting of the full-reloading curve starting from point a (y_a, x_a), which is located on the straight line passing origin *0* and reversing point r (i.e., point *1*), expressed by

$$\frac{y-y_a}{n}=f\left(\frac{x-x_a}{n}\right) \tag{2}$$

If a pair of *primary loading curves* (PLCs) in opposite shearing directions is symmetric, coefficient n becomes two. In that case, the full-reloading curve (Eq. (2)) rejoins the original PLC at point r (i.e., point *1*) without a discontinuity in the tangent modulus. On the other hand, any reloading curve starting at a certain point between points *1* and a (Eq. (1)) rejoins the original primary loading curve at point r with a discontinuity in the tangent modulus.

Fig. 5(a) schematically shows the stress–strain (y–x) relations during primary loading and the unload/reload cycles with the common maximum stress point in which the stress amplitude increases with cyclic loading, that are obtained from Eq. (1) with a constant n. With actual geomaterials, n may not necessarily be equal to two and

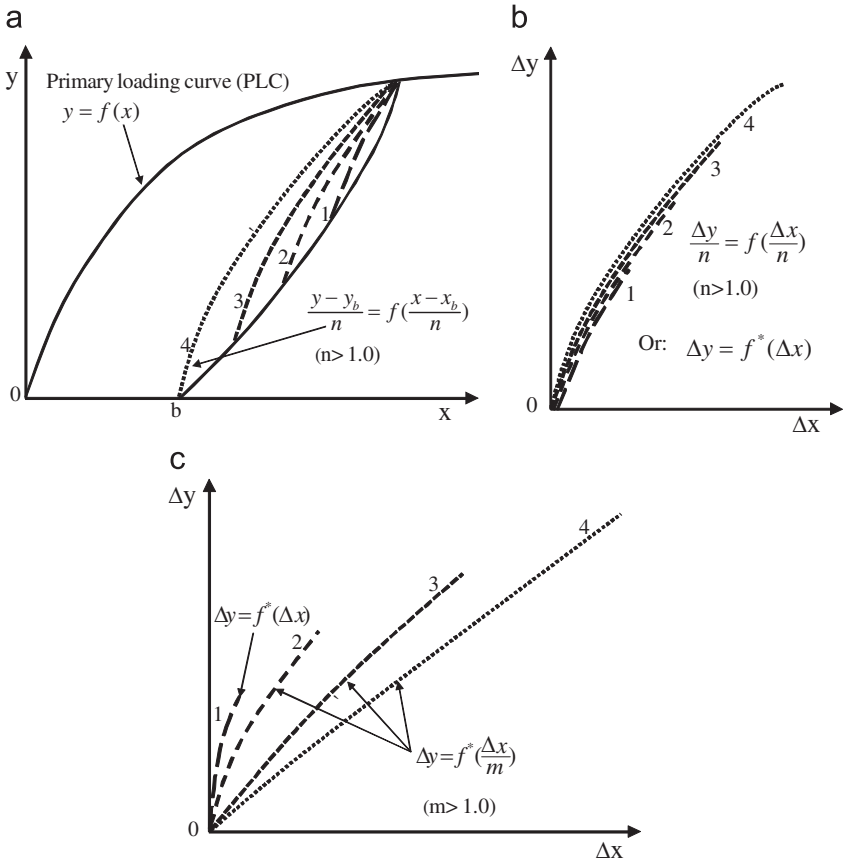

Fig. 5. (a) Stress–strain relations during primary loading and unload/reload cycles with different stress amplitudes according to Eq. (1) with a constant n, (b) re-plot of reloading relations in (a) shifted to start from common origin (i.e., Eq. (3)), and (c) reloading relations shifted to start from common origin according to Eq. (5) with m increasing from 1.0 with cyclic loading.

may change with cyclic loading. With a constant n, as shown in Fig. 5(b), all the reloading curves of which the origins have been shifted to the common origin are represented by the following single equation:

$$\frac{\Delta y}{n} = f\left(\frac{\Delta x}{n}\right) \tag{3}$$

where Δy and Δx are the increments in stress and strain since the start of reloading. Eq. (3) can be rewritten as

$$\Delta y = f^*(\Delta x) \tag{4}$$

4.2. Damage by unloading to reloading behavior

Fig. 6(a)–(e) compares the measured PLCs and the *measured reloading curves* (MRCs) whose origins of reloading have been shifted to the same origin at $q=0$ (corresponding to Fig. 5(b)). The MRCs become softer with increases in the negative axial strain increments during the respective immediately preceding unloading regimes associated with an increase in the unloaded increment of q. On the other hand, it is thought that the damage effects on the first MRCs (I-1, II-1 and III-1), for the smallest amplitude of cyclic deviator stress at different cyclic loading stages (I, II and III) in the respective tests, are negligible. By representing these first MRCs by Eq. (4), the second and subsequent MRCs were fitted by Eq. (5) as

$$\Delta y = f^*\left(\frac{\Delta x}{m}\right) \tag{5}$$

where m is the scaling parameter, equal to unity for the first MRCs or larger than unity. A larger m value means more damage to the bonding during unloading in the sense that the MRC becomes softer. In so doing, the top portion of the respective MRCs, when approaching the reversing point from which the unloading was started, is ignored. This is because this portion has become rather soft due to the increased viscous effects. Fig. 7 shows the relationship between the m value and the negative irreversible axial strain increment ($\Delta\varepsilon_a^{ir} < 0$) that took place during the unloading stage immediately preceding the concerned reloading stage. To obtain these irreversible axial strains, the elastic modulus obtained from minute unload/reload cycles applied in the respective tests, reported by Taheri et al. (2012), was used. The m–($-\Delta\varepsilon_a^{ir}$) relation is rather unique for different σ'_h values and for a wide range of ε_a^{ir} from which cyclic loading was started. The relation is rather linear and can be fitted by the following equation:

$$m = 1.0 + 11.0(-\Delta\varepsilon_a^{ir}) \tag{6}$$

where $\Delta\varepsilon_a^{ir}$ is a percentage and negative. Fig. 8(a)–(e) compares the PLC with the reloading curves modified by scaling down

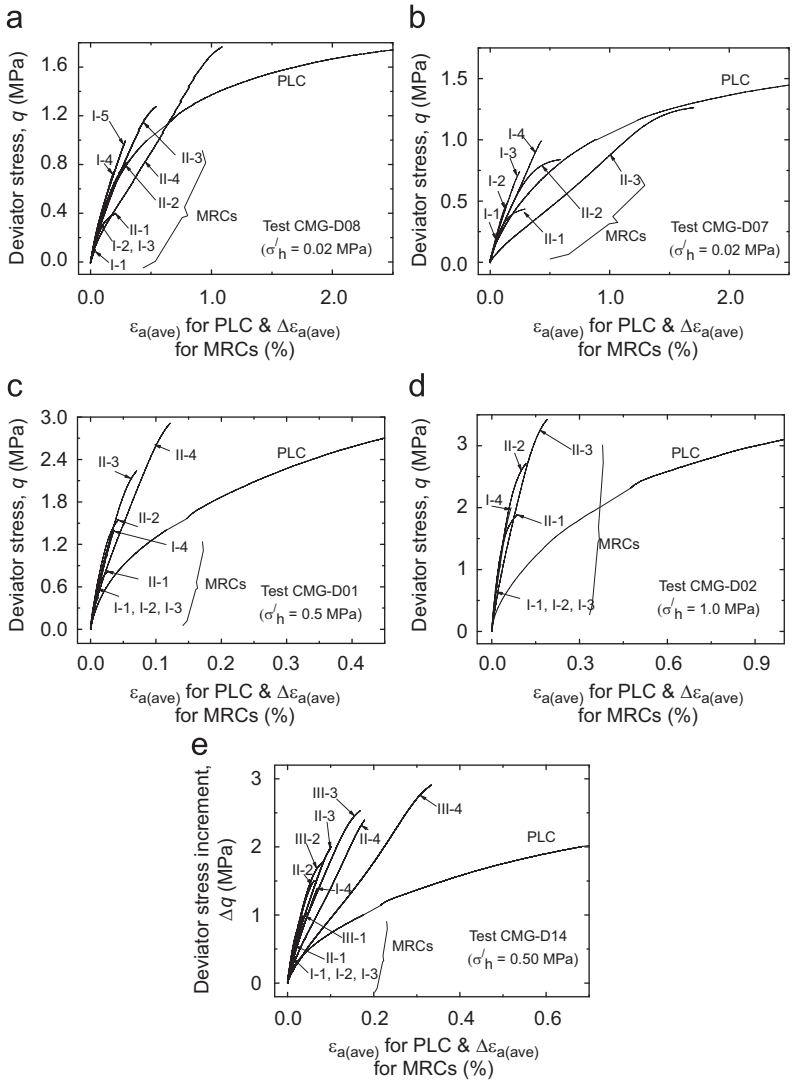

Fig. 6. Comparison of MRCs with PLC for same origin: (a) Test CMG-D08 σ'_h=0.02 MPa), (b) Test CMG-D07 (σ'_h=0.02 MPa), (c) Test CMG-D01 (σ'_h=0.5 MPa), (d) Test CMG-D02 (σ'_h=1.0 MPa), and (e) Test CMG-D14 (σ'_h=0.5 MPa).

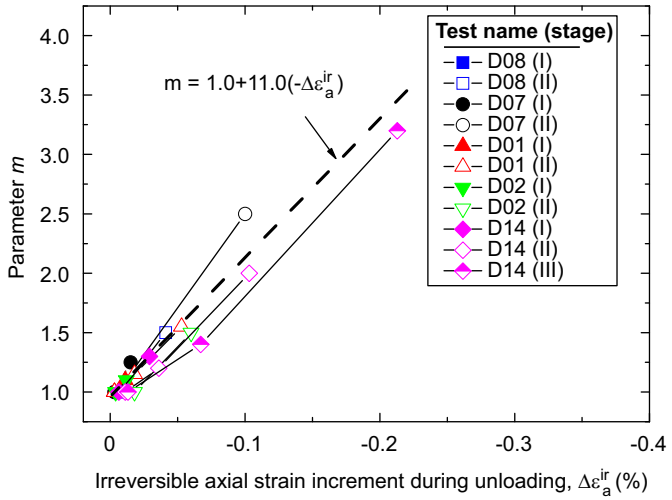

Fig. 7. Relationship between scaling parameter m and irreversible negative axial strain increment during unloading.

the axial strain increment by being divided by the parameter m obtained by substituting the respective measured $\Delta\varepsilon_a^{ir}$ values into Eq. (6). The modified unloading relations at different cyclic loading stages I, II and III have become rather unique, except for a small top part in each test. The reloading curves presented in Fig. 8 are defined as the *undamaged reloading curves* (URCs).

Based on the fact that the relation presented in Fig. 7 is rather unique for different σ'_h values, it is reasonable to assume that Eq. (6) is also valid for reloading applied after σ'_h has been changed. Then, a reloading stress–strain curve for a given $\Delta\varepsilon_a^{ir}$ value ($=A$) can be inferred by modifying a *measured reloading curve* (MRC) with a known value of $\Delta\varepsilon_a^{ir}$ ($=B$), as obtained from the ML tests (Fig. 2(a) and (b)), by the following method:

1. Parameters m_A and m_B are obtained by substituting values A and B, respectively, into Eq. (6).

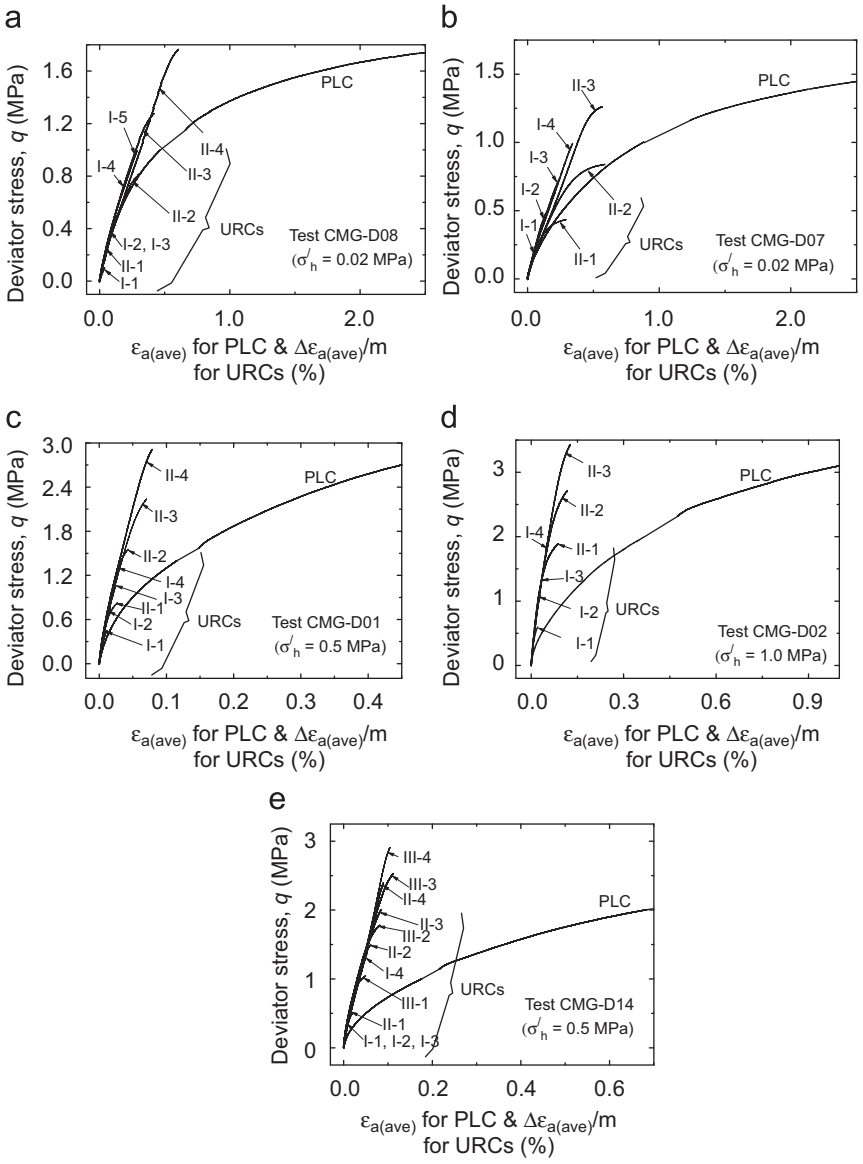

Fig. 8. Comparison of URCs with PLC for same origin: (a) Test CMG-D08 (σ'_h=0.02 MPa), (b) Test CMG-D07 (σ'_h=0.02 MPa), (c) Test CMG-D01 (σ'_h=0.5 MPa), (d) Test CMG-D02 (σ'_h=1.0 MPa), and (e) Test CMG-D14 (σ'_h=0.5 MPa).

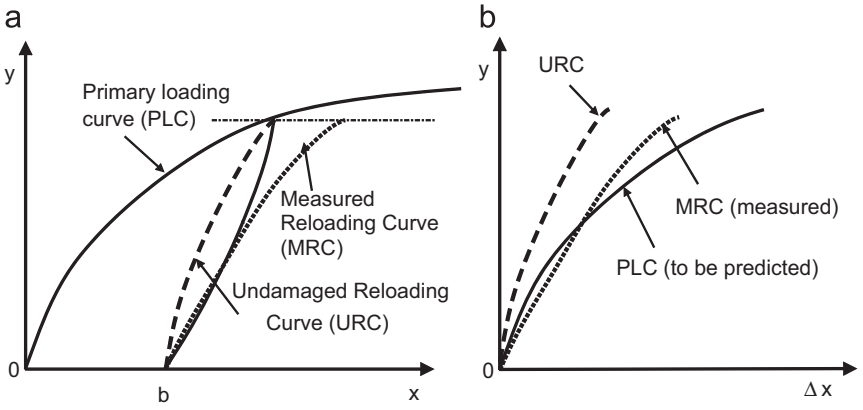

Fig. 9. (a) Primary loading curve (PLC), measured reloading curve (MRC) and undamaged reloading curve (URC) obtained by Eq. (6) and (b) re-plot of three curves in (a) from common origin.

2. Function f^*, for URC (Eq. (4)), is obtained by substituting $m=m_B$ into Eq. (5) that is fitted to the given MRC.

3. The reloading curve for the value of A is obtained by substituting $m=m_A$ into Eq. (5) of which function f^* is obtained above.

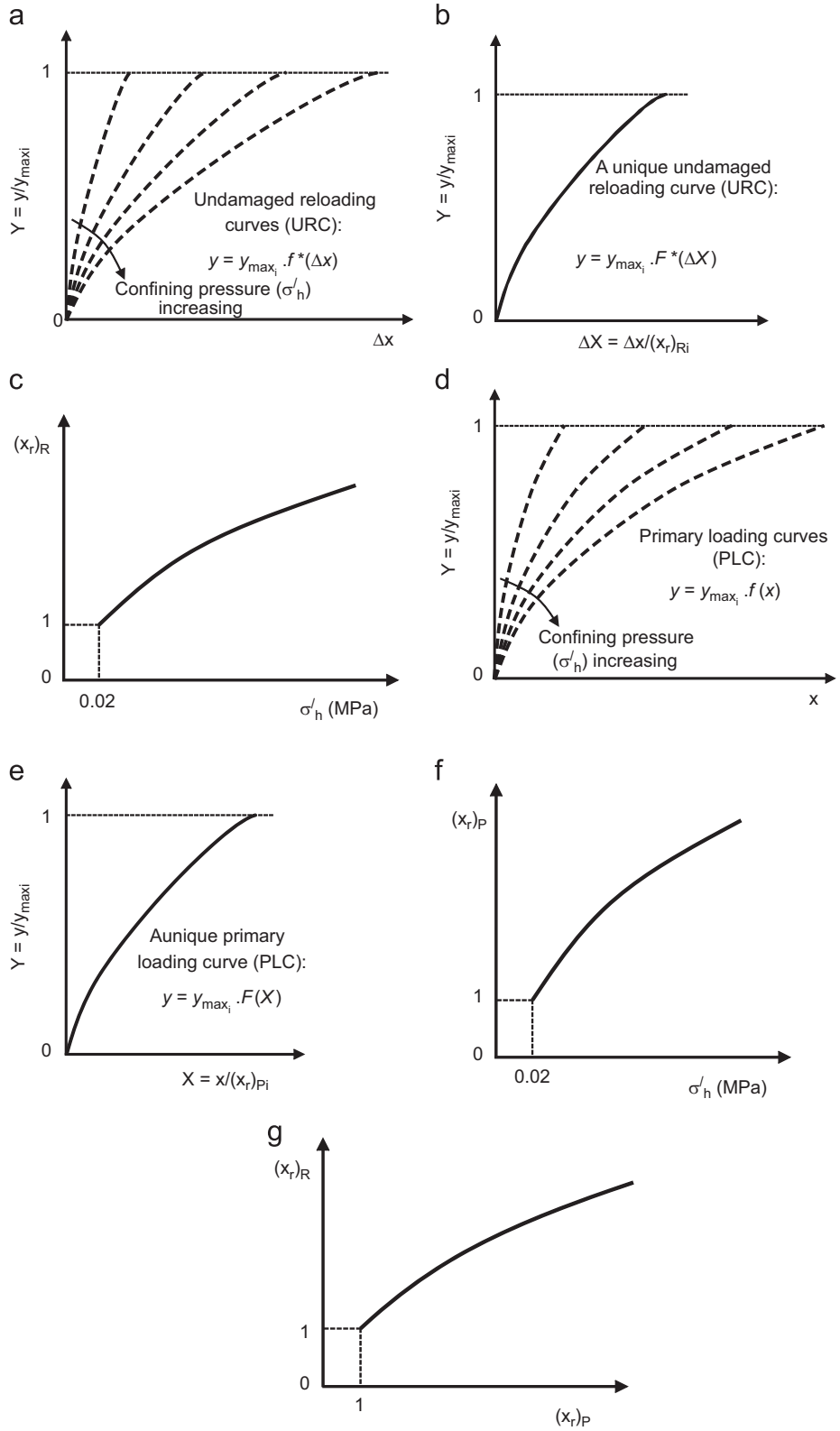

Fig. 10. Procedure to infer PLCs from reloading curves from an ML test: (a) URC at different σ'_hs, (b) unique normalized URC, (c) relationship between σ'_h and normalization factor $(x_r)_R$, (d) PLCs at different σ'_hs, (e) unique normalized PLC, (f) relationship between σ'_h and normalization factor $(x_r)_P$, and (g) relationship between normalization factors for URCs and PLCs.

When applying this method to other cases, it is recommended that the validity of Eq. (6) be examined by performing the Series 3 tests, if possible.

5. Deduction of primary loading stress–strain curves

Fig. 9(a) schematically compares a PLC with a measured full unloading curve, and presents the corresponding MRC

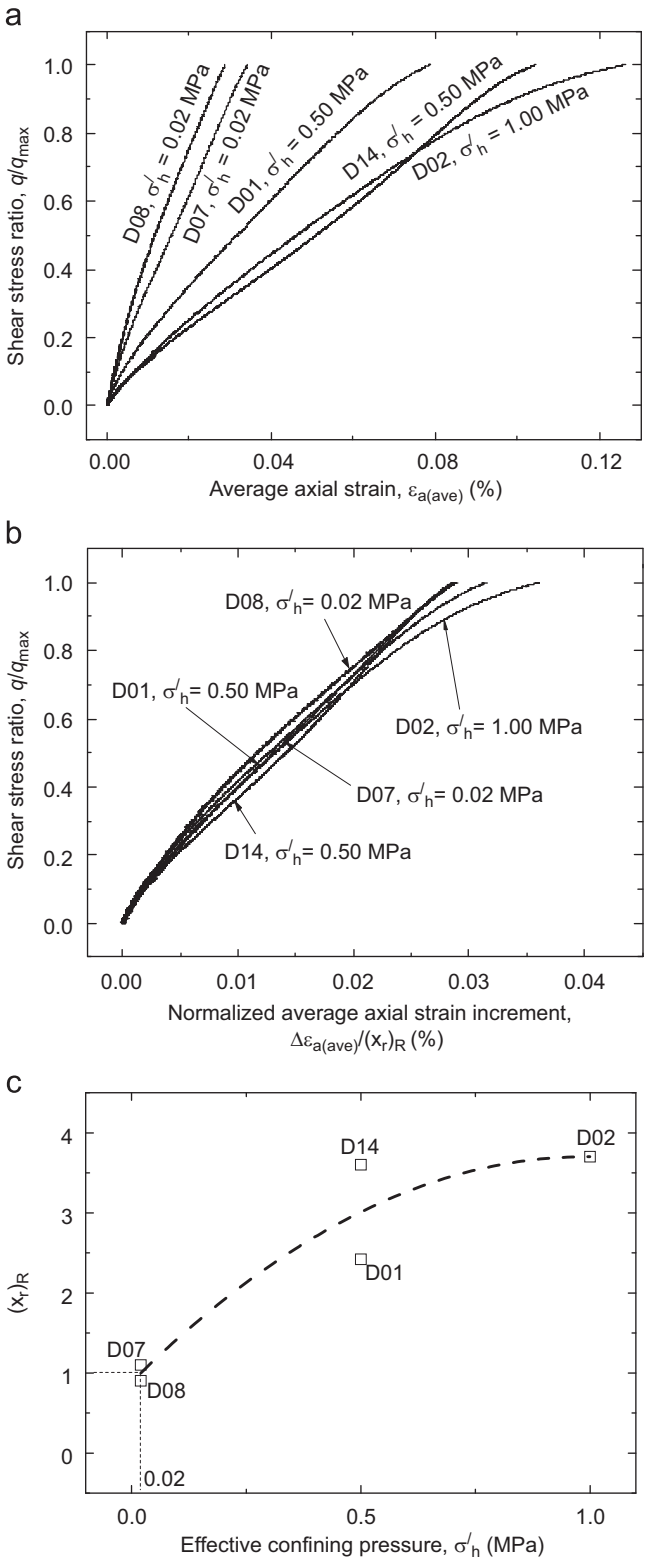

Fig. 11. (a) Shear stress ratio–axial strain increment relations for URCs, (b) shear stress ratio–normalized axial strain increment relations, and (c) relationship between σ'_h and normalization scaling factor $(x_r)_R$.

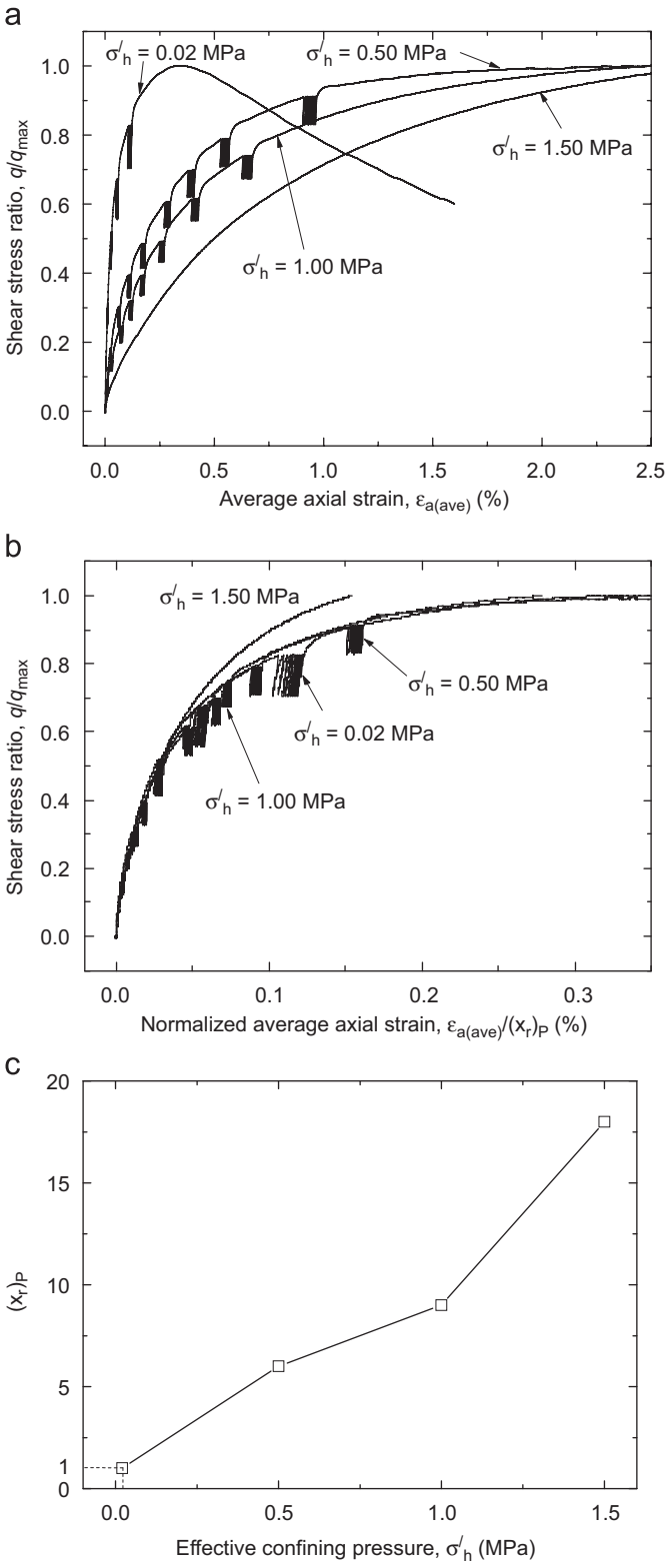

Fig. 12. (a) Primary shear stress ratio–axial strain relations from SL TCs (PRCs), (b) shear stress ratio–normalized axial strain relations, and (c) relation between σ'_h and normalization scaling factor $(x_r)_P$.

and URC obtained based on Eqs. (5) and (6). Fig. 9(b) shows that the PLC, MRC and URC shifted to the same origin. A method to infer a set of PLCs from a given set of URCs, taking into account the strain-hardening effect and the hysteresis effect on the respective URCs, is investigated. In so doing, the cyclic strain-hardening effects and the viscous effects were ignored. In this method, first, a set of PLCs at different confining pressures are extrapolated by scaling the axial strain of the PLC at the first step in a given ML test using a scaling factor obtained from an average relationship between the scaling factors for URCs and PLCs. Then, the inferred PLCs are modified by referring to the stress–strain relation after the start of large-scale yielding observed during reloading at respective confining pressures in the ML test.

5.1. Description of the procedure

(a) Fig. 10(a) schematically shows the URCs at different σ_h's obtained by the procedure explained above. $Y\ (=y/y_{max})$ is "the stress" normalized by being divided by the maximum stress. With the test results presented in Fig. 2, except for the first loading step in the ML decreasing σ'_h (explained later), y_{max} is the maximum deviator stress measured at each loading step. The peak strength at the first step in the ML test decreasing σ'_h was inferred based on the SL test results. Fig. 11(a) shows the actual data from the Series 3 tests. Some scatter seen in the data is due to an inevitable variance among the different specimens tested. Similar to the behavior in the SL tests with the same plotting method (Fig. 12(a)), the stress–strain behavior becomes softer with an increase in σ'_h in this form of plotting (i.e., the stress ratio y/y_{max} versus the axial strain increment Δx). The respective URCs at different confining pressures are expressed as.

$$y = y_{max_i}.f^*(\Delta x) \tag{7}$$

(b) Fig. 10(b) shows the URCs after scaling down axial strain increment Δx by dividing a normalization scaling factor $(x_r)_R$ to obtain the normalized axial strain increment $X=\Delta x/(x_r)_R$, where "$(x_r)_R$ when $\sigma'_h=0.02$ MPa"$=1.0$ so that a unique normalized URC relation is obtained regardless of σ'_h. Fig. 11(b) shows the actual normalized rations obtained from the data presented in Fig. 11(a). This unique relation is expressed as

$$y = y_{max_i}.F^*(\Delta X) \tag{8}$$

(c) Fig. 10(c) shows the relationship between the normalization factor $(x_r)_R$ and σ'_h. Fig. 11(c) shows the actual data. All the $(x_r)_R$ values at the different σ'_h values were obtained so that the average of the two data at $\sigma'_h=0.02$ MPa would be equal to 1.0. The scatter seen in Fig. 11(a) is reflected in the scatter in the $(x_r)_R$ values in Fig. 11(c). The average relation is used in the analysis explained below.

(d) Fig. 10(d) illustrates the PLCs at different fixed σ'_h values from a set of SL tests. Fig. 12(a) shows the actual data. Similar to the URCs presented in Fig. 10(a), with an increase in σ'_h, the stress–strain behavior becomes softer in this form of plotting. The respective PLCs are

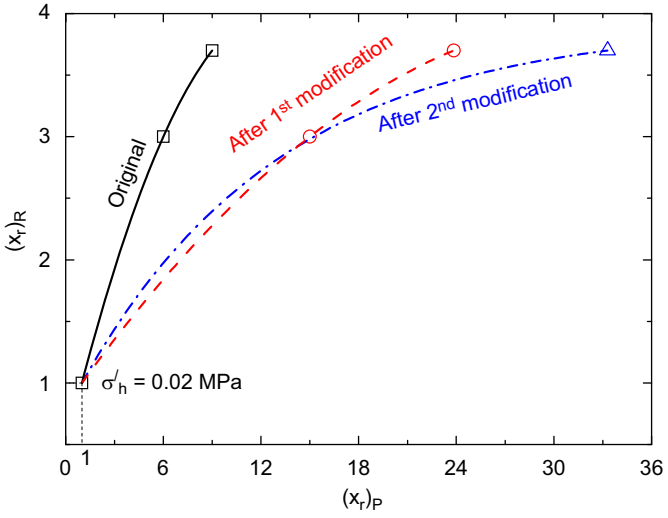

Fig. 13. Relations between two normalization factors.

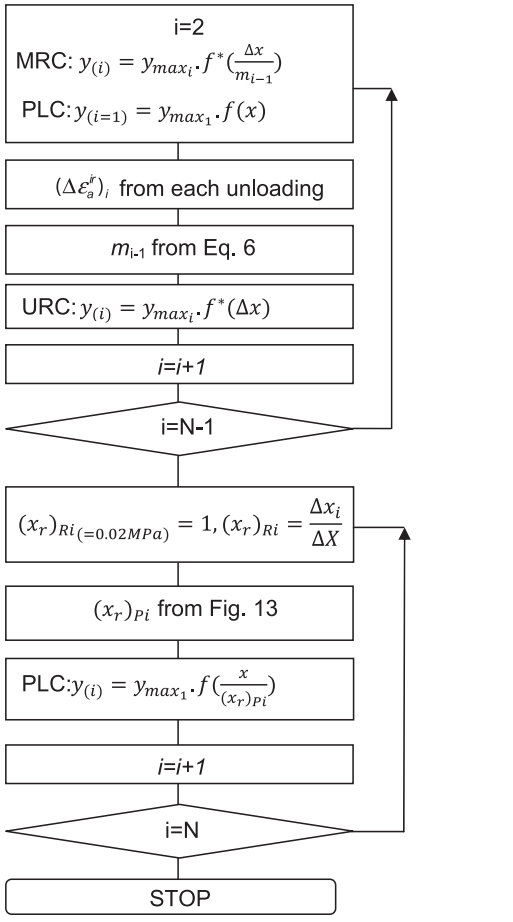

N: number of loading steps in an ML test

Fig. 14. Procedure to infer PLCs from MRCs.

represented by

$$y = y_{max_i} . f(x) \quad (9)$$

(e) Fig. 10(e) shows the PLCs after scaling down axial strain x by another normalization scaling factor, $(x_r)_P$, where "$(x_r)_P$ when σ'_h =0.02 MPa"=1.0 so that a unique normalized PLC relation is obtained regardless of σ'_h. This unique relation is expressed as

$$y = y_{max_i} . F(X) \quad (10)$$

where $X=x/(x_r)_P$. Fig. 12(b) shows the actual data.

(f) Fig. 10(f) shows the relationship between normalization factor $(x_r)_P$ and σ'_h. Fig. 12(c) shows the actual data.

(g) Fig. 10(g) shows the relationship between normalization scaling factors $(x_r)_R$ and $(x_r)_P$ at the different identical confining pressures. Fig. 13 shows the actual data (denoted as 'Original'). This relation is used to infer the PLCs at different σ'_h values from the PLC measured at the first loading step and the URCs measured at the second and subsequent loading steps in a given ML test.

PLCs at different σ'_hs that are higher than the lowest σ'_h (at the first loading step) are inferred by extrapolating the PLC at the first loading step. As the extent of extrapolation becomes very large, when deducing the PLCs at confining pressures much higher than the lowest σ'_h (at the first loading step), the accuracy of the deductions may become low. Moreover, there could be some variance among the data sets from the three series of tests that are used in this analysis. Consequently, the PLCs inferred at Step (g) are modified based on the part of PLC observed at stresses after the start of the large-scale yielding in the respective reloading regimes in the ML test of which the data are used to infer the PLCs (shown by thick black curves in Fig. 2(a)). The modification method will be explained in detail later in this paper.

5.2. Examination by experimental data

PLCs at different σ'_h values were inferred from the PLC at the first loading step of an ML test using a single specimen referring to the MRCs at different σ'_h values obtained from the ML test. Fig. 14 shows this procedure.

The proposed method was applied first to the ML test increasing σ'_h presented in Fig. 2(a). The m value for the respective MRCs at the second and subsequent loading steps was obtained by substituting the negative irreversible axial strain increments ($\Delta\varepsilon_a^{ir}$) during the immediately preceding unloading into Eq. (6). The *undamaged reloading curves* (URCs) were obtained by dividing the measured axial strain increments by the respective m values. Fig. 15(a) shows the URCs in terms of the shear stress ratio (q/q_{max}) – axial strain increment ($\Delta\varepsilon_a$) relations at σ'_h=0.25, 0.50, 0.75 and 1.0 MPa obtained from the data

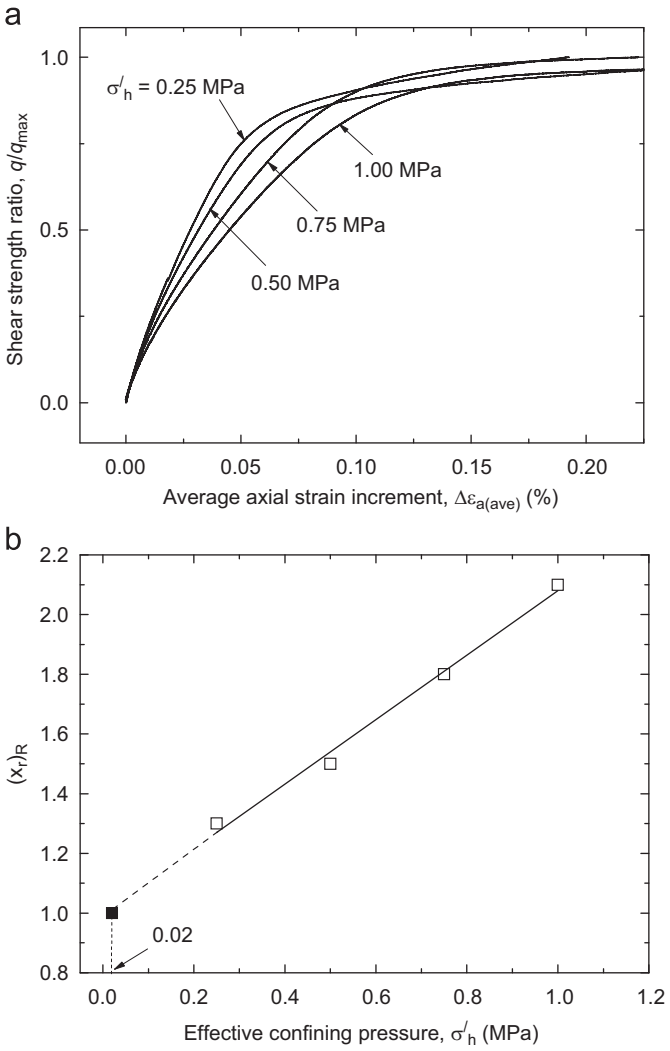

Fig. 15. (a) URCs from the ML test increasing σ'_h and (b) relationship between $(x_r)_R$ and σ'_h.

of the ML test increasing σ'_h. The stress–strain relations become softer with an increase in σ'_h. However, the dependency on σ'_h is much smaller than the one with the URCs from the Series 3 tests (i.e., a set of cyclic loading tests at different confining pressures using multiple specimens), presented in Fig. 11(a). Therefore, the variation in the $(x_r)_R$ values presented in Fig. 15(b) is much smaller than the one in Fig. 11(b). This may be due partly to the cyclic strain-hardening effects, discussed in Introduction, in that the stiffness increases by repeating the full unload/reload cycles performed with different σ'_h in the ML test and partly to a variance among the specimens used in the three series of tests.

Then, under the condition whereby the normalization factor $(x_r)_R$=1.0 at σ'_h=0.02 MPa, the $(x_r)_R$ values at the higher σ'_h values were calculated so that all the URCs became unique, as shown in Fig. 15(b). In this figure, a linear relation is fitted to the data. The normalization factor $(x_r)_P$ for the PLCs was obtained by substituting the respective $(x_r)_R$ values into the original relation shown in

Fig. 13. Finally, the PLCs at the σ'_h values at the second and subsequent loading steps (=0.25, 0.50, 0.75 and 1.0 MPa) were obtained by scaling up "the axial strain of the PLC at the first step at σ'_h=0.02 MPa" by a factor of $(x_r)_P$ at the respective confining pressures. Fig. 16(a) shows the inferred PLCs together with the measured one at the first loading step (σ'_h=0.02 MPa). The dependency on σ'_h of the inferred PLCs is obviously smaller than the one of the PLCs observed in the SL tests (Fig. 12(a)).

Fig. 17(a)–(d) compares these inferred and measured PLCs and measured MRCs at different σ'_h values. The following trends may be seen. First, the MRCs are generally stiffer than the PLCs measured by the SL tests. This is due to the fact that the positive effects of the strain-hardening phenomenon are more dominant than the negative effects of the damage taking place during the immediately preceding unloading scheme. Second, the inferred PLCs are generally stiffer than the measured PLCs. That is, in Fig. 17(a), although the PLC at σ'_h=0.25 MPa inferred based on the original relation in Fig. 13 lies between the PLCs measured at σ'_h=0.02 and 0.5 MPa (Fig. 12(a), tests CB3-1 and CB3-6), it is located much closer to the one measured at σ'_h=0.02 MPa. This indicates that the stiffness of the inferred PLC at σ'_h=0.25 MPa is overestimated. Moreover, the inferred PLC at σ'_h=0.5 MPa is considerably stiffer than the one observed in an SL test (Fig. 17(b)). The inferred PLC at σ'_h=0.75 MPa is even stiffer than the one measured at σ'_h=0.5 MPa (Fig. 17(c)) and, at σ'_h=1.0 MPa, the inferred PLC is a poor approximation of the results measured in an SL test (Fig. 17(d)). This inconsistency can be confirmed from Fig. 18(a)–(d). The respective data points in these figures denote the E_{tan} value determined from the test results. In these figures, at each stage of σ'_h=0.25, 0.5, 0.75 and 1.0 MPa in the ML test increasing σ'_h, at stresses exceeding the yield stress during reloading, the E_{tan} values of the inferred PLC are much higher than those measured. These two sets of E_{tan} values should be the same if the original relation presented in Fig. 13 is relevant.

In Fig. 19, the PLC measured at σ'_h=0.02 MPa, at the first step in the ML test increasing σ'_h from which the PLCs at higher σ'_h s were inferred, is compared with the one measured at σ'_h=0.02 MPa in an SL test (Fig. 12(a), Test CB3-1). The difference between the two relations is insignificant. Besides, the former is even slightly softer than the latter. Therefore, this difference is not a cause for the trends of inconsistency discussed above. A very large extent of extrapolation from the PLC at the lowest σ'_h (0.02 MPa) to those at much higher σ'_hs and some variance among the specimens used in the three series of tests (discussed in the preceding sections) may be among other factors causing this large inconsistency.

5.3. Modification

It is obvious that the confining pressure-dependency of the $(x_r)_P$ obtained by substituting the $(x_r)_R$ values presented in Fig. 15(b) into the original $(x_r)_R$–$(x_r)_P$ relation presented in

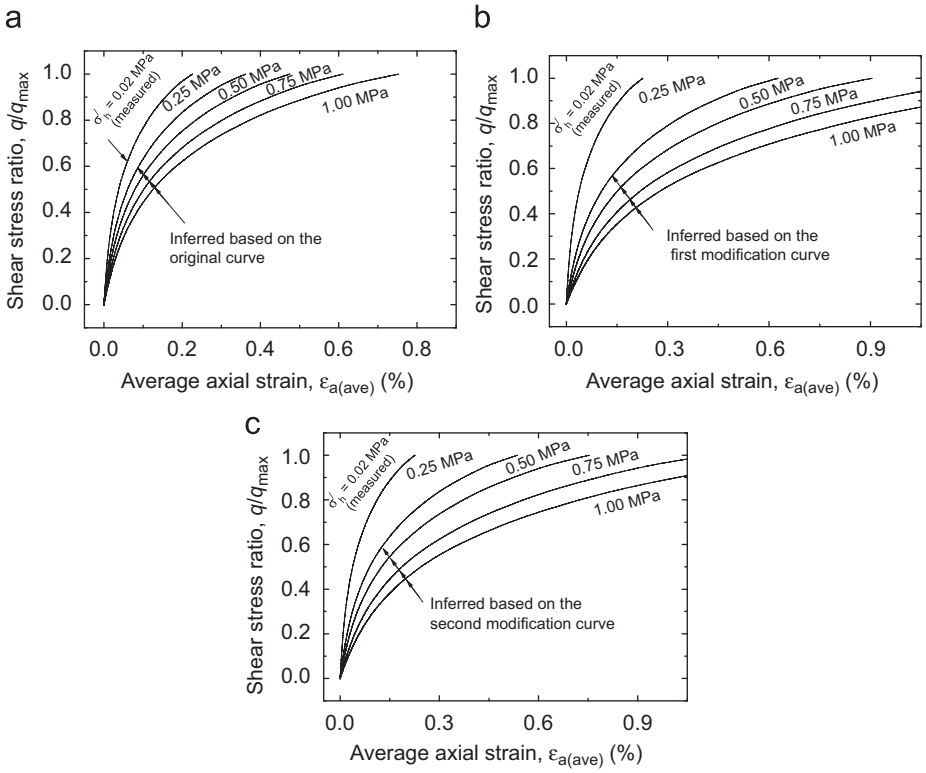

Fig. 16. PLC measured at σ'_h=0.02 MPa and PLCs at other σ'_hs inferred from results of an ML test increasing σ'_h (by procedure shown in Fig. 14) obtained based on (a) original curve, (b) first modified curve, and (c) second modified curve in Fig. 13.

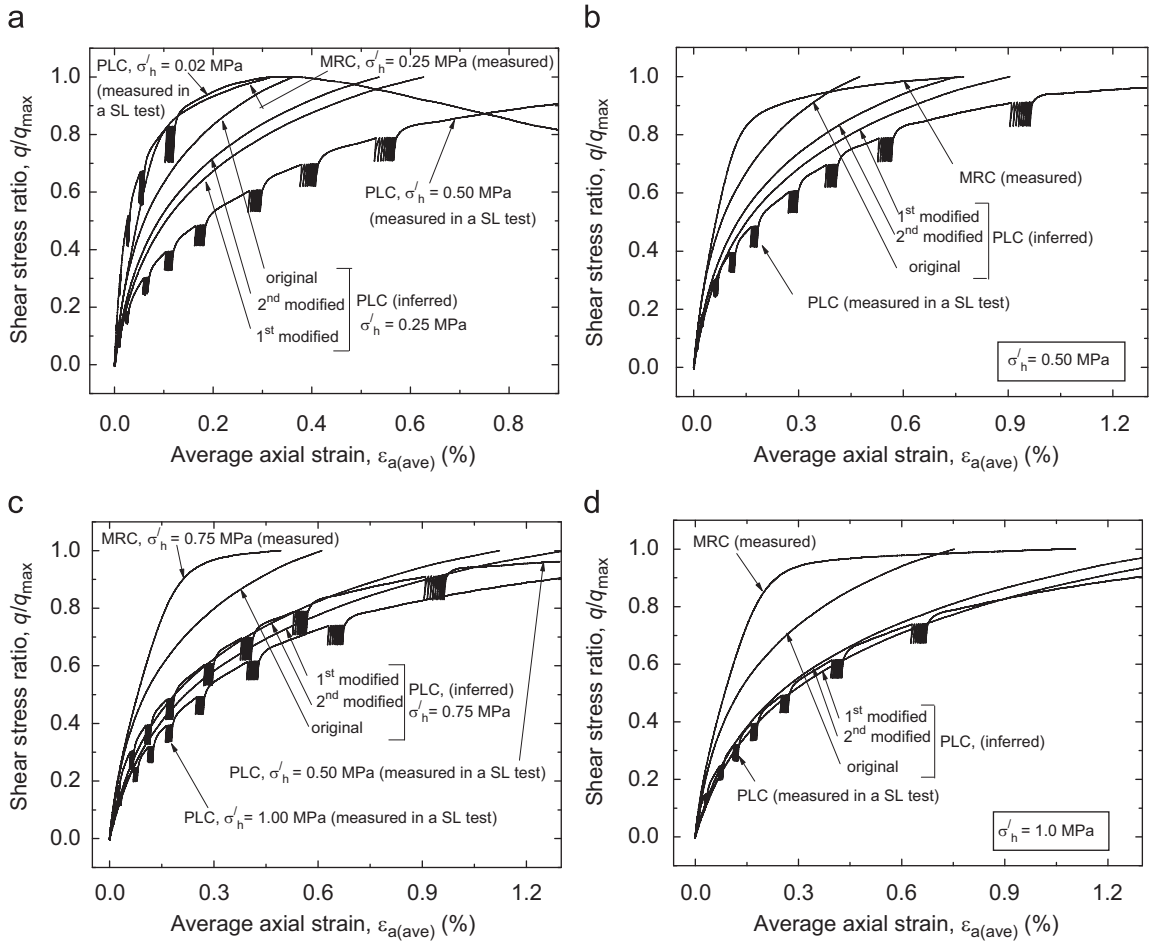

Fig. 17. Comparison of PLCs inferred by basic method from results of an ML test increasing σ'_h (following procedure shown in Fig. 14) at σ'_h=(a) 0.25 MPa, (b) 0.50 MPa, (c) 0.75 MPa, and (d) 1.00 MPa with measured PLCs from SL tests.

Fig. 13 is too small. The original relation presented in Fig. 13 is therefore modified below based on the results presented in Fig. 18(a)–(d). Note that this modification uses only the data from the ML test of which the data is used to infer PLCs. In each of Fig. 18(a)–(d), the dashed line indicates the primary loading relation below the yield stress inferred by extrapolating the measured primary loading relation above the yield stress. Differences between these relations and the PLCs, inferred based on the original relation in Fig. 13, indicate how much the inferred PLC should be modified to the correct one in each case. Fig. 20 shows the ratio between the average of the E_{tan} values at stresses exceeding the yield stress along the PLC, inferred based on the original relation (Fig. 13), and the one of the corresponding measured E_{tan} values at respective σ'_h values, $(E_{tan(inferred)}/E_{tan(measured)})$, obtained from the plots in Fig. 18(a)–(d). The average ratio is generally significantly higher than 1.0, i.e., 1.46 at σ'_h=0.25 MPa, about 2.5 at σ'_h=0.50 and 0.75 MPa, and 3.7 at σ'_h=1.0 MPa. Based on the above, the relation given in Fig. 13 is modified by the following two approaches of modification.

First approach: The value of $(x_r)_P$ of the original curve in Fig. 13 is increased by a factor that is equal to the average of the four $E_{tan(inferred)}/E_{tan(measured)}$ ratios, equal to 2.5.

Second approach: The two available data of the $(x_r)_P$ value at $(x_r)_R$=3.0 (σ'_h=0.5 and 0.75 MPa) and the one at $(x_r)_R$=3.7 (σ'_h=1.0 MPa) of the original relation were made larger by a factor of the respective average ratios of E_{tan} , equal to 2.5 and 3.7.

In Fig. 13, a non-linear curve was fitted to each set of two data of the $(x_r)_R$–$(x_r)_P$ relation, as denoted by the first and the second modifications.

Fig. 16(b) and (c) shows the PLCs inferred based on the modified curves presented in Fig. 13. The dependency of PLC on the confining pressure is much larger than those inferred based on the original curve (Fig. 16(a)), while similar to the one of the PLCs observed in the SL tests (Fig. 12(a)). It may be seen from Fig. 17(a)–(d) that the PLCs inferred based on the modified relations (Fig. 13) are much more consistent with the measured ones. The difference between the PLCs inferred based on the first and second approaches of modification is not significant. Therefore, the first modified curve is used below to infer PLCs from the data of the ML test decreasing σ'_h presented in Fig. 2(b).

The proposed method was then applied to the ML test decreasing σ'_h, in which drained TC was performed first at σ'_h=1.0 MPa and reloading was repeated atσ'_h=0.75, 0.5, 0.25 and 0.02 MPa. The results of the analysis following

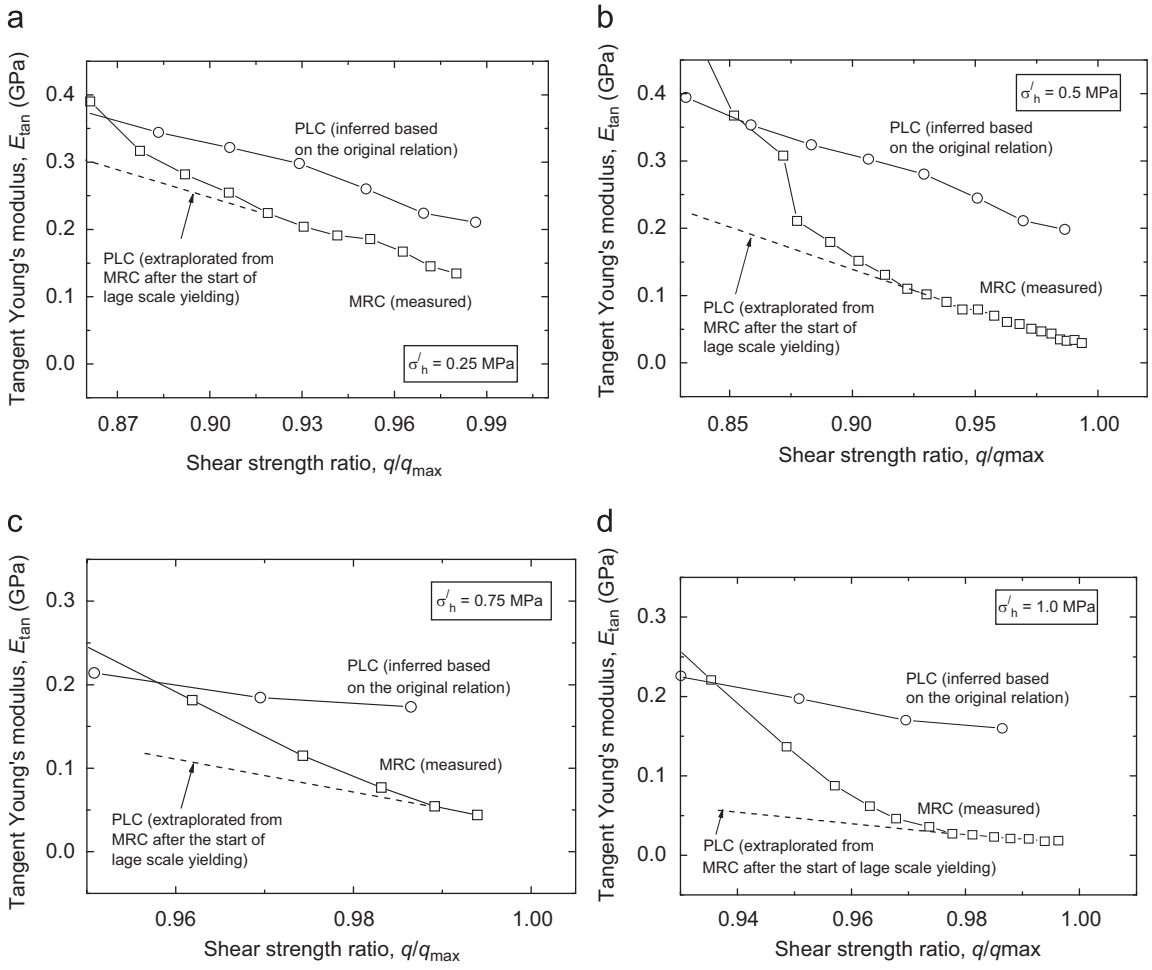

Fig. 18. Comparison of tangent Young's modulus during reloading in the ML test increasing σ'_h between inferred and measured PLCs: (a) σ'_h=0.25 MPa, (b) σ'_h=0.50 MPa, (c) σ'_h=0.75 MPa, and (d) σ'_h=1.00 MPa.

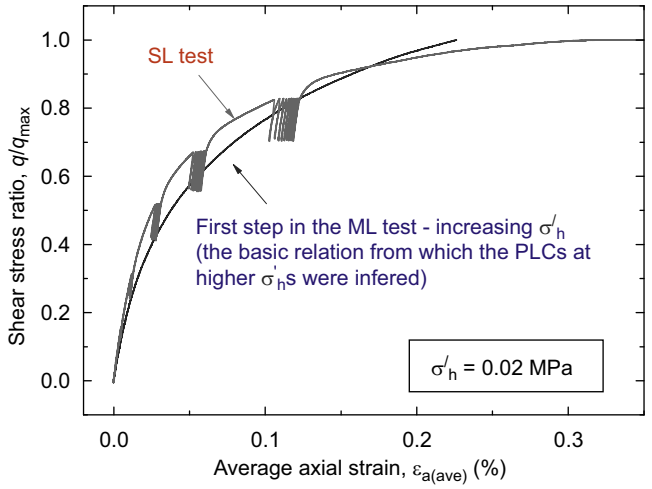

Fig. 19. Comparison of PLCs at σ'_h=0.02 MPa from the ML test increasing σ'_h and the SL test.

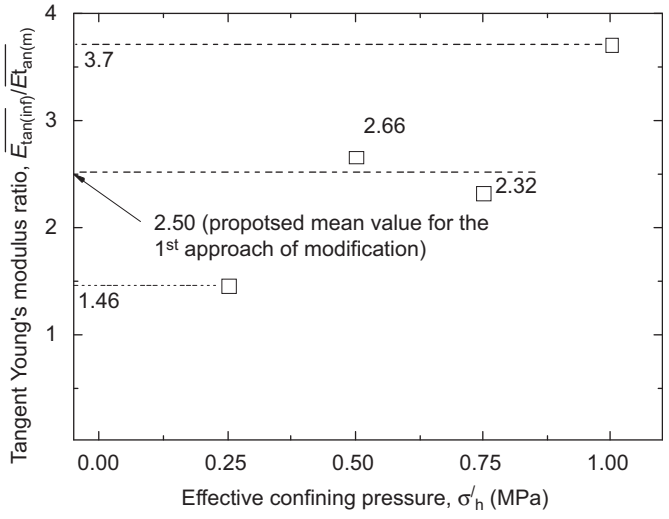

Fig. 20. Relationships between tangent Young's modulus ratio and effective confining pressure (σ'_h) from the ML test increasing σ'_h.

the procedure described in Fig. 14, using the first modified curve of the $(x_r)_R$–$(x_r)_P$ relation in Fig. 13, are presented below. Note that an analysis, such as that presented in Figs. 18 and 20, cannot be performed with the data of this test, as the large-scale yielding started in the post-peak regime during reloading except for σ'_h=0.75 MPa (Fig. 2(b)).

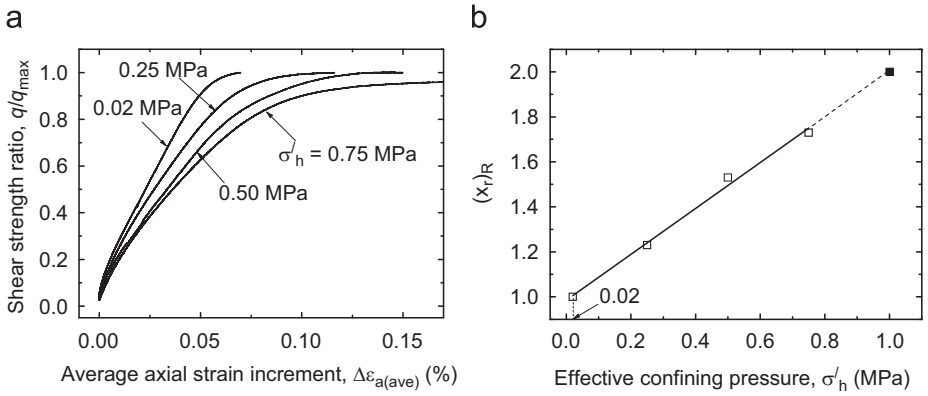

Fig. 21. (a) URCs from the ML test decreasing σ'_h and (b) relationship between $(x_r)_R$ and σ'_h.

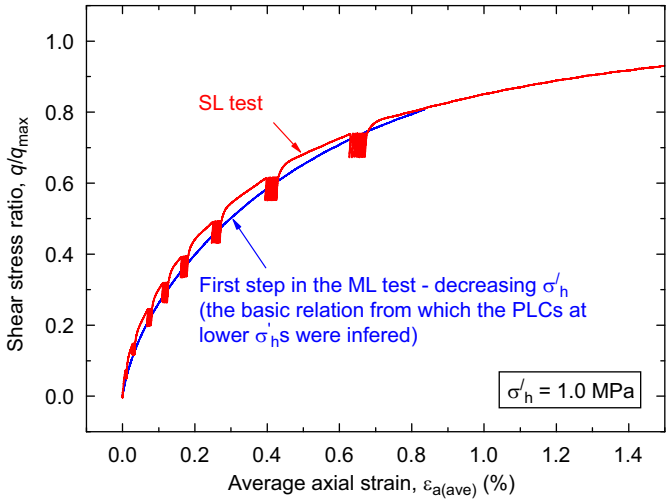

Fig. 22. Comparison of PLCs at σ'_h=1.0 MPa from the ML test decreasing σ'_h and SL tests.

Fig. 21(a) shows the URCs obtained from the MRCs using Eq. (6). The dependency on σ'_h of these URCs is similar to the ML test increasing σ'_h (Fig. 15(a)). In Fig. 21(b), the normalization scaling factors, $(x_r)_R$, determined so that the URCs presented in Fig. 21(a) become unique under the condition that $(x_r)_R$=1.0 at σ'_h=0.02 MPa are plotted against σ'_h. The obtained relation is rather linear. In Fig. 22, the PLC at σ'_h=1.0 MPa, measured at the first stage of this ML test from which the PLCs at lower σ'_hs are inferred, is compared with the one measured in an SL test (Fig. 12(a), Test CB3-8). The fact that these two stress–strain relations are very similar indicates that a comparison of the PLCs inferred from the former with those measured by SL tests shown below is relevant.

Fig. 23(a) shows the PLC measured at the first step (σ'_h=1.0 MPa) of this ML test and the PLCs at σ'_h=0.02, 0.25, 0.5 and 0.75 MPa inferred by scaling down the axial stain of this PLC measured at σ'_h=1.0 MPa by a factor of $(x_r)_P$ obtained by substituting the $(x_r)_R$ values presented in Fig. 21(b) into the first modified curve (Fig. 13). The q_{max} value at the first step (σ'_h=1.0 MPa) in this ML test was 3.31 MPa, which was significantly lower than the peak value measured in the corresponding SL test CB3-8 (q_{peak}=4.10 MPa). Therefore, q_{peak}=4.10 MPa was used as the q_{max} value to obtain the ratio q/q_{max} in this plot. The dependency of these inferred PLCs on σ'_h is similar to the one of the PLCs measured in the SL tests (Fig. 12(a)). Fig. 23(b)–(e) compares these inferred PLCs in the pre-peak regime at different σ'_hs with the corresponding measured PLCs from SL tests. It may be seen that the inferred PLCs are consistent with those measured by the SL tests. By the nature of the method used to infer these PLCs, the post-peak regime cannot be inferred.

5.4. The suggested method

A reasonable comparison of the PLCs, inferred from the results of a pair of ML tests increasing and decreasing σ'_h with those measured by SL tests, indicates that the method proposed is basically relevant. This method first uses two empirical relations, namely, (i) Eq. (6) (Fig. 7) and (ii) the first modified curve presented in Fig. 13. Further study is necessary to examine the generality of these two empirical relations with other types of soft rock.

When this method is applied to infer PLCs at different σ'_hs, from given data of an ML test increasing σ'_h in other cases, if these empirical relations are not available, the following method can be suggested:

1. The URC is obtained from a given MRC based on Eq. (6); this procedure is repeated for different σ'_h values.
2. Values for parameter $(x_r)_R$, at different σ'_h values, are obtained to have a unique URC.
3. Values for parameter $(x_r)_P$ are obtained by substituting these $(x_r)_R$ values into the first modification curve presented in Fig. 13.
4. PLCs at different σ'_hs are inferred using these $(x_r)_P$ values by scaling the axial strains of a given measured PLC measured at the first step of the ML test increasing σ'_h.
5. The stress–strain relations after the start of the large scale yielding, during (the) reloading at different σ'_h values in the ML test, are analyzed, as shown in Figs. 18 and 20, for comparison with the data of the inferred PLCs.
6. The $(x_r)_R$–$(x_r)_P$ relation is modified based on the above analysis.

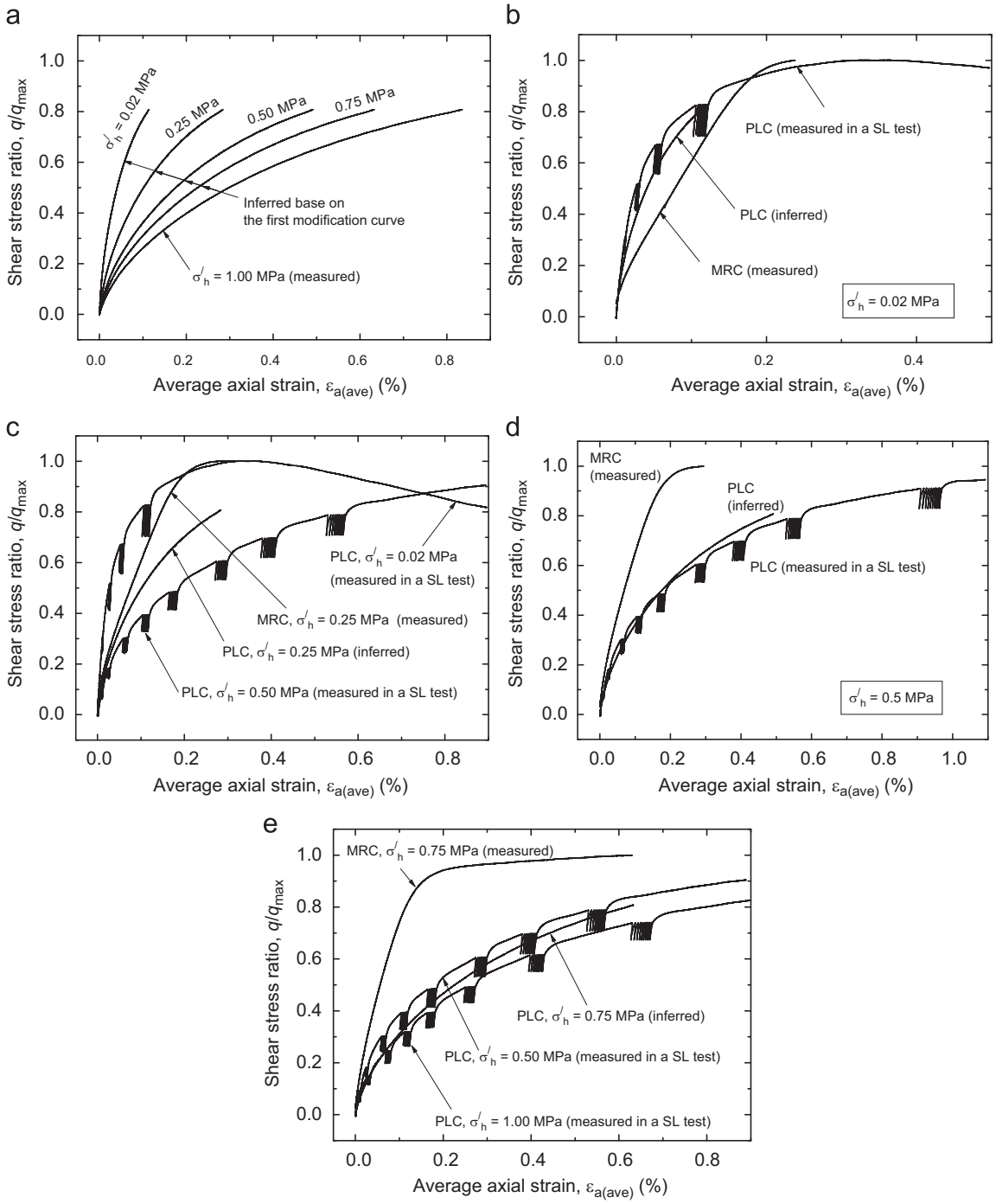

Fig. 23. (a) Measured PLC at σ'_h=1.0 MPa and PLCs at other σ'_hs inferred based on first modification curve from the ML test decreasing σ'_h and comparison of PLCs inferred by basic method at σ'_h=: (b) 0.02 MPa, (c) 0.25 MPa, (d) 0.5 MPa, and (e) 0.75 MPa with measured PLCs from SL tests.

7. Repeat Step (4) using the $(x_r)_R$–$(x_r)_P$ relation obtained in Step (6).

6. Conclusions

The following conclusions can be drawn from the analysis presented above:

1. In drained triaxial compression (TC) tests on a cement-mixed gravelly soil (CMG), the stress–strain relations during reloading were seen to become proportionally softer along with the increase in negative axial strain increments that had taken place during the immediately preceding unloading regime. This trend was expressed by an empirical equation to infer the undamaged reloading stress–strain relations from a given reloading relation.
2. A method was developed within the framework of the proportional rule to infer primary loading curves (PLCs) at different confining pressures (σ'_hs) from the

PLC at the first step in given multiple-step loading (ML) TC tests referring to the reloading stress–strain curves measured at different σ'_hs in the ML tests. The PLCs inferred above were then modified based on the post-yielding stress–strain relations measured during reloading at different σ'_hs in the ML test.

This method was validated by comparing the PLCs inferred from the results of a pair of ML tests increasing and decreasing σ'_h with those obtained from single-step loading (SL) TC tests performed at different σ'_hs.

Acknowledgments

The first author is grateful to the Japan Society for the Promotion of Science for the fellowship (ID No. P08392) supporting this research and to Tokyo University of Science for the post-doctorial fellowship.

References

Aoki, H., Yonezawa, T., Watanabe, O., Tateyama, M., Tatsuoka, F., 2003. Results from field full-scale loading tests on a bridge abutment with backfill of geogrid-reinforced cement-mixed gravel. Geosynthetics Engineering Journal 18, 237–248 Japanese Chapter of International Geosynthetics Society, in Japanese.

Ezaoui, A., Tatsuoka, F., Sano, Y., Iguchi, Y., Maeda, Y., Sasaki, Y., Duttine, A., 2010. Ageing effects on the yielding characteristics of cement-mixed granular materials. Soils and Foundations 50 (5), 705–724.

Ezaoui, A., Tatsuoka, F., Taheri, A., Sasaki, Y., Furusawa, S., Arakawa, K., 2011. Size effects on the strength properties of low cement-mixed granular soils. In: 46th Japan Geotechnical Society Conference (JGS), pp. 629–30.

Goto, S., Tatsuoka, F., Shibuya, S., Kim, Y.S., Sato, T., 1991. A simple gauge for local small strain measurements in the laboratory. Soils and Foundations 31 (1), 169–180.

Hansen, K.D., Reinhardt, W.G., 1990. Roller-Compacted Concrete Dams, McGraw-Hill, Inc.

Kongsukprasert, L., Tatsuoka, F., 2003. Viscous effects coupled with aging effects on the stress–strain behavior of cement-mixed gravel. In: Di Benedetto, et al. (Eds.), Proceedings of 3rd International Conference on Pre-Failure Deformation Characteristics of Geomaterials, vol. 1, Lyon, Balkema, pp. 569–577.

Kongsukprasert, L., Tatsuoka, F., 2005. Ageing and viscous effects on the deformation and strength characteristics on cemented-mixed gravelly soil in triaxial compression. Soils and Foundations 45 (6), 55–74.

Kongsukprasert, L., Tatsuoka, F., 2007. Small strain stiffness and non-linear stress–strain behavior of cemented-mixed gravelly soil. Soils and Foundations 47 (2), 375–394.

Kongsukprasert, L., Tatsuoka, F., Tateyama, M., 2005. Several factors affecting the strength and deformation characteristics cement-mixed gravel. Soils and Foundations 45 (3), 107–124.

Lohani, T.N., Kongsukprasert, L., Watanabe, K., Tatsuoka, F., 2004. Strength and deformation properties of cemented-mixed gravel evaluated by triaxial compression tests. Soils and Foundations 44 (5), 95–108.

Masuda, T., Tatsuoka, F., Yamada, S., Sato, T., 1999. Stress–strain behavior of sand in plane strain compression, extension and cyclic loading tests. Soils and Foundations 39 (5), 31–45.

Schrader, E.K., 1996. Compaction of Roller Compacted Concrete, ACI. Special Publication (SP96-6), pp. 77–101.

Taheri, A., Sasaki, Y., Tatsuoka, F., 2011. Effects of cyclic pre-shearing on the stress–strain behavior of cemented-mixed gravel. In: Proceedings of 5th International Conference on Deformation Characteristics of Geomaterials, pp. 334–341.

Taheri, A., Sasaki, Y., Tatsuoka, F., Watanabe, K., 2012. Strength and deformation characteristics of cemented-mixed gravelly soil in multiple-step triaxial compression. Soils and Foundations 52 (1), 151–170.

Tatsuoka, F., 2004. Cement-mixed soil for Trans-Tokyo Bay highway and railway bridge abutments, In: Yegian, Kavanzanjian (Eds.), Proceedings of GeoTrans 04, GeoInstitute, ASCE Special Geotechnical Publication SPT No. 126), Los Angeles, pp. 18–76.

Tatsuoka, F. and Kohata, Y. (1995): Stiffness of hard soils and soft rocks in engineering applications. In: Shibuya et al. (Eds.), Keynote Lecture, Proceedings of International Symposium Pre-Failure Deformation of Geomaterials, Balkema, vol. 2, pp. 947–1063.

Tatsuoka, F., Jardine, R. J., Lo Presti, D., Di Benedetto, H., Kodaka, T., 1999. Characterization the pre-failure deformation of geomaterials. In: Theme Lecture for the Plenary Session No. 1, Proceedings of. 14th ICSMFE, Hamburg, 1997, vol. 4, pp. 2129–2164.

Tatsuoka, F., Masuda, T., Siddiquee, M.S.A., 2003. Modelling the stress–strain behavior of sand in cyclic plane strain loading. Journal of Geotechnical and Environmental Engineering, ASCE 129 (No. 6, June 1), 450–467.

Tatsuoka, F., Tateyama, M., Aoki, H., Watanabe, K., 2005. Bridge abutment made of cement-mixed gravel backfill. In: Indradratna, Chu (Eds.), Ground Improvement, Case Histories, Elesevier Geo-Engineering Book Series, vol. 3, pp. 829–873.

Tatsuoka, F., Di Benedetto, H., Kongkitkul, W., Kongsukprasert, L., Nishi, T., Sano, Y., 2008. Modeling of ageing effects on the elasto-viscoplastic behavior of geomaterial. Soils and Foundations 48 (2), 155–174.

Watanabe, K., Tateyama, M., Jiang, G., Tatsuoka, F., Lohani, T.N., 2003. Strength characteristics of cement-mixed gravel evaluated by large triaxial compression tests. In: Di Benedetto et al. (Eds.), Proceedings of 3rd International Conference on Pre-Failure Deformation Characteristics of Geomaterials, Lyon, Balkema, vol, 1, pp. 683–693.

Watanabe, K., Tateyama, M., Yonezawa, T.Aoki, H., 2005. Strength characteristics and construction management of cement-mixed gravel. In: Proceedings of 16th International Conference on Soil Mechanics and Geotechnical Engineering, IS-OSAKA, pp. 619–622.